Preprints of the 21st IFAC World Congress (Virtual)
Berlin, Germany, July 12-17, 2020

Impact of Sensor Placement on Mode Observability and LQG Control of a Thermoacoustic System

Xiaoling Chen * **Hosam Fathy** ** **Jacqueline O'Connor** ***

* *Department of Mechanical Engineering, Pennsylvania State University, University Park, PA 16802 USA, (e-mail: xpc5020@psu.edu)*
** *Department of Mechanical Engineering, University of Maryland, College Park, MD 20742 USA, (e-mail: hfathy@umd.edu)*
*** *Department of Mechanical Engineering, Pennsylvania State University, University Park, PA 16802 USA, (e-mail: jxo22@psu.edu)*

Abstract: This paper investigates the effect of sensor placement on the observability and LQG control of a thermoacoustic model. This model describes combustion instability in a one-dimensional combustor, called a Rijke tube. The transfer function describing this model is transcendental because of the time delay terms in the heat release dynamics. We apply Padé approximation to achieve a finite-dimensional transfer function and truncate the system by neglecting states with low Hankel singular values. We then analyze the impact of the placement and number of sensors on the observability of each mode of the resulting reduced-order model. Next, we design an LQG controller for suppressing pressure oscillations in the simplified thermoacoustic system. We find that placing sensors near the model's pressure nodes slows down the rate at which LQG control attenuates pressure oscillations, increases the control effort required for this attenuation, and worsens the controller's robustness.

Keywords: Thermoacoustic system, Padé approximation, Hankel singular value, Linear-Quadratic-Gaussian, sensor placement, μ analysis.

1. INTRODUCTION

This paper examines the impact of sensor placement in a one-dimensional combustor on the problem of observing and controlling thermoacoustic instability within the combustor. Combustion instability is a problematic phenomenon occurring in lean premixed combustion systems. It usually manifests itself in the form of large-amplitude pressure oscillations. These oscillations can lead to flame extinguish and, in extreme cases, system hardware vibrations [Lieuwen and Yang (2005)]. The cause of combustion instability is a positive feedback coupling between the combustor acoustics and heat release rate oscillations from flame [Lieuwen et al. (1999)].

Combustion instabilities can be attenuated by passive [Richards et al. (2003)], phase-shift [Langhorne et al. (1990)], or model-based active controls. In these controls, sensors such as pressure transducers [Lang et al. (1987)] and photo-detectors [Hermann et al. (1999)] can identify the instability. The actuators are usually speakers providing acoustic forcing [Dines (1984), Heckl (1988), Lang et al. (1987), Poinsot et al. (1989)], variations in the acoustic boundary conditions [Bloxsidge et al. (1988), Bothien et al. (2008)], or additional fuel injections [Hermann et al. (1999), Barooah et al. (2003)] to break the coupling between combustor acoustics and flame heat release dynamics.

Sensor configuration is one important factor that affects the performance of combustion stability controls. The literature presents a number of studies examining the effect of sensor placement on combustion stability control. Control techniques examined in this literature include phase shift control [Lang et al. (1987)], state feedback control, pole placement [Yang et al. (1992)], acoustic boundary condition control [Bothien et al. (2008), Zhao and Li (2012)], and LQG control [Annaswamy and Ghoniem (1995),Hathout et al. (1998), Annaswamy et al. (2000)]. The metrics used for evaluating these controllers' performance usually include control effort [Annaswamy and Ghoniem (1995), Hathout et al. (1998), Annaswamy et al. (2000)], objective cost function values (for both controlled and residual modes) [Yang et al. (1992)], pressure peak attenuation [Annaswamy et al. (2000)], settling time [Hathout et al. (1998), Annaswamy et al. (2000)], and stability domains [Lang et al. (1987), Poinsot et al. (1989)].

One common insight in the literature is that for active combustion stability control, sensor location should ideally be near the pressure anti-node of the fundamental acoustic mode. See, for example, Lang et al. (1987). Smaller control gains are also achieved if the actuator is closer to the pressure anti-node as seen in phase-gain plane analysis [Poinsot et al. (1989)]. Similarly, one study applied LQG control and achieved system stabilization with a reduction of control effort by 30% when the sensor was moved to a better location [Annaswamy and Ghoniem (1995)]. In

addition to a lower control effort, some studies also found that collocated sensor-actuator pairs achieve a shorter settling time compared to the non-collocated case [Hathout et al. (1998), Annaswamy et al. (2000)]. Yang et al. [Yang et al. (1992)] found that the optimal sensor location is exactly the same as the optimal actuator location, which is between the first nodal points of the lowest and highest residual modes. There is one successful application of active instability control at an industrial scale, which occurred in a Model V84.3A gas turbine [Seume et al. (1997)], where a direct-drive valve responsible for a pilot flame was controlled to suppress the single frequency oscillation. The pressure oscillation amplitude decreases by 86% with optimal sensor placement and the smallest number of sensors along the circumferential coordinate.

Stability robustness of a controller is another important assessment criterion in addition to performance. Annaswamy et al. [Annaswamy et al. (2000)] applied both LQG-LTR and H_∞ to control the combustion instability in a lean-premixed combustion rig with a range of equivalence ratios and flow rates. They found that though H_∞ is more sluggish with a longer settling time in suppressing the instability than LQG-LTR, it has a better robustness. A similar conclusion is found by Lang et al. [Lang et al. (1987)] that a smaller gain for the phase-shift controller is required when sensor is closer to the pressure anti-node, but this control suffers from uncertainty in the phase information.

Based on the literature, we recognize that sensor placement plays a significant role in determining both the performance and robustness of a controller designed to suppress combustion instabilities. The optimal sensor location seems to be at the anti-node of the dominant acoustic mode(s). The performance and robustness of different controllers have also been compared in the literature.

The overarching goal of this paper is to provide further examination of the impact of sensor placement on: (i) the observability of the different modes of a one-dimensional combustor; (ii) the performance of an LQG controller designed to suppress thermoacoustic instability in this combustor; and (iii) the robustness of this LQG controller. We perform this analysis based on an experimentally-identified model of the combustor's thermoacoustic dynamics. Moreover, in performing the robustness portion of this analysis, we explicitly account for the uncertainties in the experimentally-identified values of this model's parameters.

The structure of the paper is as follows. Section 2 describes the thermoacoustic model for the one-dimensional combustor and the experimental system identification results. Section 3 describes a linear finite dimensional thermoacoustic model by a multi-point Padé approximation. In the same section, we analyze the effects of sensor placement and number of sensors on the Hankel singular values of the further reduced-order system. In analyzing the effects of the number of sensors, we apply a sequential optimization scheme to find the optimal combination of the multiple sensors. For the further reduced-order system, we design an LQG controller in section 4 to suppress the pressure oscillations. This section further discusses the dependence of both performance and robustness of the LQG controller on the sensor placement and number of sensors with a similar analysis scheme as that in section 3, followed by conclusions summarized in section 5.

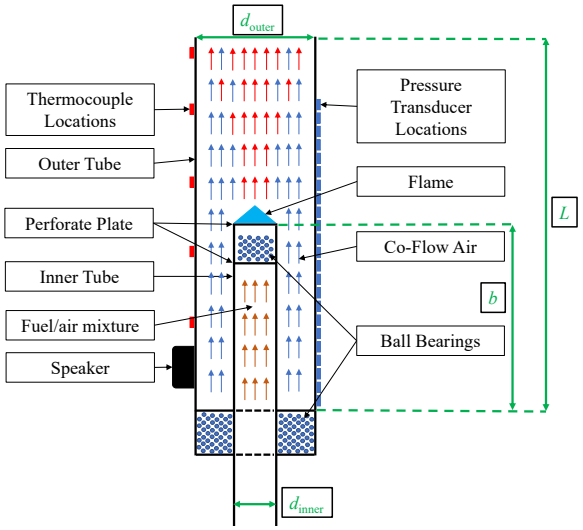

Fig. 1. Rijke tube cross-section schematic

2. COMBUSTION INSTABILITY MODEL

2.1 Rijke Tube Experiment Setup

In this paper, we develop a thermoacoustic model and identify the model with a Rijke tube setup shown in Fig.1. This configuration consists of two tubes. The outer tube has a length of $L = 0.875m$ and a diameter of $d_{outer} = 0.091m$. The inner has a diameter of $d_{inner} = 0.022m$. A methane-air mixture flows through the inner tube, stabilizing a laminar flame with an equivalence ratio of 0.8 on the top, with the help of a perforate plate and ball bearings to provide uniform flows. The flame location b, defined as the distance between the inner tube top and the outer tube inlet, can be changed by sliding the inner tube upward or downward.

Near the outer tube inlet, a speaker is mounted to provide acoustic forcing either as the system identification or control input. The tube exit is open to the atmosphere, as a pressure release boundary. Along the Rijke tube height, multiple uniformly distributed discrete locations are available to implement pressure transducers and thermocouples. The bottom measurement location is at $0.041m$ and the uniform gap is $0.027m$ between adjacent locations.

2.2 Thermoacoustic Model

For simplicity, we describe the Rijke tube with a one-dimensional thermoacoustic model by neglecting radial and azimuthal variations; we consider independent variables time t and axial coordinate x. Further, due to the heat release from combustion, the temperatures in regions upstream and downstream of the flame are assumed to be different constants $\bar{T}_1$ and $\bar{T}_2$, respectively. As a result, the mean density $\bar{\rho}$ and speed of sound $\bar{c}$ are at two different constants in the two regions, too. We also assume the mean flow to be isentropic, homogeneous, and steady. Additionally, the amplitudes of the oscillating variables including

pressure p', velocity u', and density ρ' are assumed to be small compared with their corresponding mean values for linearization. The linearized governing equations that describe the conservation of mass, momentum, and energy are as follows.

$$\frac{\partial \rho'}{\partial t} + \bar{\rho}\frac{\partial u'}{\partial x} = 0,\ \bar{\rho}\frac{\partial u'}{\partial t} = -\frac{\partial p'}{\partial x} \tag{1}$$

$$\frac{\partial p'}{\partial t} = -\bar{\rho}\bar{c}^2\frac{\partial u'}{\partial x} + (\gamma - 1)q' \tag{2}$$

In (2), variable q' represents the fluctuation of heat release rate per unit volume and γ is the specific heat capacity ratio. We apply a linear time-lag model from Ref. Crocco and Cheng (1956) to describe the heat release dynamics, as indicated in the following equation. This model accurately captures flame response at least in linear dynamics region.

$$q'(x,t) = Q'(t)\delta(x-b),\ Q'(t) = -\frac{\beta\bar{\rho}\bar{c}^2}{\gamma - 1}u_1'(t-\tau) \tag{3}$$

The right equation above describes the linear time-lag response of the heat release oscillation per unit area Q' to the incoming flow perturbations u_1'. Parameter β is the amplification factor and τ is the time delay. The left equation represents the acoustically compact flame at location b by a Dirac delta function $\delta(x-b)$.

We describe the two boundary conditions in Fig. 1 by the following equation. One represents the acoustic forcing at the tube inlet and the other represents the pressure release boundary at the tube outlet.

$$u'(0,t) = u_0'(t),\ p'(L,t) = 0 \tag{4}$$

Taking the spatial derivative of the right equation in (1) and the time derivative of equation (2), rearranging them considering equation (3) leads to a non-homogeneous acoustic wave equation describing the pressure oscillations.

$$\frac{\partial^2 p'}{\partial t^2} - \bar{\rho}\bar{c}^2\frac{\partial}{\partial x}\Big(\frac{1}{\bar{\rho}}\frac{\partial p'}{\partial x}\Big) = \frac{\beta\bar{\rho}\bar{c}^2}{\bar{\rho}_1}\delta(x-b)\frac{\partial p_1'(t-\tau)}{\partial x} \tag{5}$$

For the PDE in frequency domain (s) after Laplace transform, we can achieve the analytical solution of the pressure oscillation $P'(x,s)$ from a perspective of continuous spatial domain. From system perspective, the pressure $P'(x,s)$ can be regarded as local output of the thermoacoustic system with the input from the acoustic forcing $U_0'(s)$, a Laplace domain input corresponding to $u_0'(t)$ in time domain. We then apply a transfer function between normalized input and output to describe the system.

$$\begin{aligned} H_n(x,s) \equiv& \frac{P_n'(x,s)}{U_n'(s)} \\ P_n'(x,s) = \frac{P'(x,s)}{p_{atm}},\ & U_n'(s) = \frac{U_0'(s)}{u_b} \end{aligned} \tag{6}$$

Output and input are normalized with respect to atmospheric pressure p_{atm} and bulk flow velocity u_b, respectively. Solving the PDE in (5) analytically, we obtain the system transfer functions for region upstream

$$H_n(x,s) = \frac{\bar{\rho}_1\bar{c}_1 u_b}{p_{atm}}\frac{(\bar{\rho}_1\bar{c}_1 e_{24})e^{-\frac{x}{\bar{c}_1}s} - (\bar{\rho}_1\bar{c}_1 e_{13})e^{\frac{x}{\bar{c}_1}s}}{\bar{\rho}_m\bar{c}_m e_m + \bar{\rho}_n\bar{c}_n e_n} \tag{7}$$

and region downstream of the flame

$$H_n(x,s) = \frac{\left(\bar{\rho}_m^2\bar{c}_m^2 - \bar{\rho}_n^2\bar{c}_n^2\right)e^{t_5 s}u_b\left(e^{\frac{2L-x}{\bar{c}_2}s} - e^{\frac{x}{\bar{c}_2}s}\right)}{2p_{atm}(\bar{\rho}_m\bar{c}_m e_m + \bar{\rho}_n\bar{c}_n e_n)} \tag{8}$$

In the transfer functions, terms e_{13}, e_{24}, $\bar{\rho}_m\bar{c}_m$, $\bar{\rho}_n\bar{c}_n$, e_m, e_n and t_5 are further explained in the Appendix A.

2.3 Model Identification

The two parameters τ and β governing heat release dynamics strongly affect the transfer functions, as seen in the authors' previous paper [Chen et al. (2019)]. Specifically, the transfer function magnitude is especially sensitive to the parameters near acoustic resonant frequencies. Due to the strong dependence of transfer function magnitude on the two parameters, we indirectly identify the two parameters by measuring the transfer function magnitude at frequencies that are near the acoustic resonance of the Rijke tube with setup in Fig. 1.

During parameter identifications, the sensor noise in the transfer function output measurement propagates to the parameters in terms of the estimate uncertainties. We apply Fisher identifiability analysis to optimize the experimental design that achieves estimate uncertainties as low as possible to reach the Cramér Rao lower bound [Sharma and Fathy (2014)]. Flame location significantly affects the system acoustics by determining the temperature distribution. To exclude the effects of flame location when studying the effects of sensor placement, we select two flame locations to make the analysis more general. The parameters identification are summarized in table 1.

Table 1. Model identification results for two cases

Case Design Variables	**Case 1**	**Case 2**
Flame location b (m)	0.3	0.4
Bulk flow velocity u_b (m/s)	2	2
Identification Results		
Nominal $\hat{\beta}_0$ (1)	0.8274	1.337
Nominal $\hat{\tau}_0$ (ms)	11.90	11.72
Standard deviation $\sigma_{\hat{\beta}}$ (1)	0.0030	0.0070
Standard deviation $\sigma_{\hat{\tau}}$ (ms)	0.0065	0.0043

3. EFFECT OF SENSOR PLACEMENT ON HANKEL SINGULAR VALUES

3.1 Model Order Reduction

The above system is infinite dimensional due to the time delay τ in the heat response dynamics. To make it finite dimensional, we apply multi-point Padé approximation [Celik et al. (1995)] to focus on the first few finite acoustic modes. So, we select multiple frequency points near the system's first four dominant acoustic modes and ensure moment matches between original and approximated system transfer functions at these frequency points. Similar with single point Padé approximation, the coefficients in the numerator and denominator of the approximated transfer function $H_{n,pa}(x_0, s_j)$ are determined by satisfying moment matching conditions. The number of moments near each frequency point n_k might be different depending

on the local frequency response characteristics. They are determined to achieve an overall minimal approximation error, defined as an optimization problem below in (9).

$$\begin{aligned} \underset{n_{k,(k=1,\ldots,5)}}{\textbf{min}} \quad & \Delta|H_n(x_0,s)| = \\ & \sqrt{\frac{1}{N_s}\sum_{j=1}^{N_s}[|H_n(x_0,s_j)|-|H_{n,pa}(x_0,s_j)|]^2} \\ \textbf{subject to} \quad & s_j = j2\pi f_j, f_j = 0,1,2,\ldots,800Hz \\ & N_s = \dim(f_j) \\ & 1 \le n_k \le 5, \sum_{k=1}^{5} n_k = q \end{aligned} \tag{9}$$

The objective cost function is the mean difference between the original and approximated transfer function magnitudes over the frequency range of interest. Variable N_s is the length of the frequency points vector s_j. The constraints specify the range of n_k and the total order of the approximated transfer function q. For multi-output system, multi-point Padé approximation method works similarly. In this paper, for case b=0.3m and b=0.4m, we apply 10 and 14 sensors uniformly distributed in the region upstream the flame. The orders of the approximated transfer function with the two flame locations are set to be q=20 and 24. The optimal objectives in the two cases are around 0.005, with an approximation accuracy of 95% knowing that the analytical transfer function magnitude near dominant acoustic modes is around 0.1.

3.2 Hankel Singular Value Calculation

For the approximated rational transfer function obtained after Padé approximation, we analyze the mode observability quantified by the Hankel singular values. In this paper, we assume that Padé approximation reserves the observability of the mode in the original PDE-governed system. We construct a state space model in block diagonalizing modal canonical realization form for the rational transfer function. In this form, we truncate the system with one mode remained and achieve the Hankel singular value for the single mode.

The Hankel singular values are the square roots of the eigenvalues of a matrix which is the product of the observability and controllability Gramian matrices. Repeating the truncation and Hankel singular value calculation multiple times, we can achieve the Hankel singular values for each mode. Because the system is unstable, we follow the algorithm developed in [Nagar and Singh (2004)] to analyze the mode observability in the system by referring to [Zhou et al. (1999)] instead of using MATLAB toolbox directly.

3.3 Dependence of Hankel Singular Values on Sensor Placement

For each sensor placement, we calculate the Hankel singular values of both stable and unstable dominant modes with the method in [Zhou et al. (1999)]. The dependence of the Hankel singular values of the four dominant modes

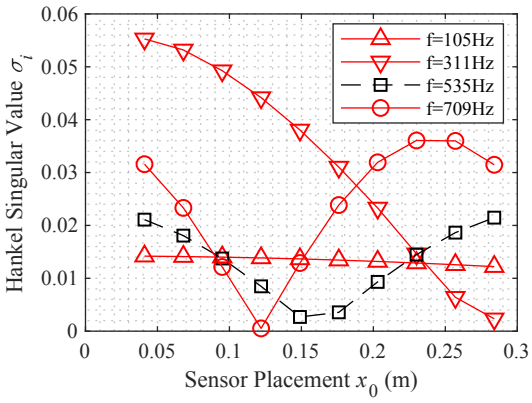

Fig. 2. Dependence of Hankel singular values for dominant modes on sensor placement in case 1, $b = 0.3m$

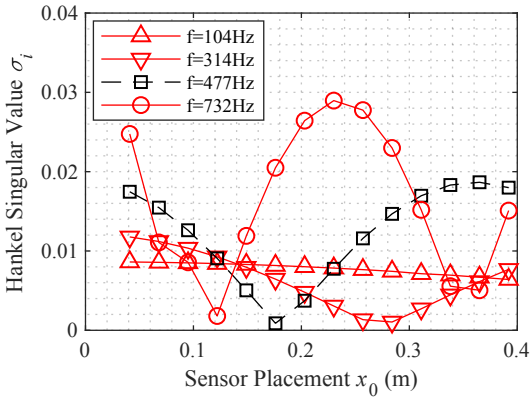

Fig. 3. Dependence of Hankel singular values for dominant modes on sensor placement in case 2, $b = 0.4m$

on the sensor placement is illustrated in Fig.2 and Fig.3 for two cases, where we already neglect the other modes with extremely small Hankel singular values.

For all the dominant modes in both cases, the dependence of the Hankel singular values on sensor placement behaves similarly with the corresponding mode shapes. There is a trade-off among multiple acoustic modes for higher observability if there is only one sensor available. For example, single sensor placement at the bottom can ensure the maximal Hankel singular value for the first and the second mode, but not for the third and the forth mode. This is one reason to study effect of multiple sensors next. Additionally, to ensure good observability especially for the unstable modes connected by the solid lines, we need to avoid placing the sensors on the pressure nodes where the Hankel singular values are close to zero. This is another reason to study the potential improvement of mode observability with multiple sensors.

3.4 Dependence of Hankel Singular Values on the Number of Sensors

To solve the observability trade-off among different modes and avoid placing sensor near the mode node, we study the dependence of mode observability on multiple sensor placements. In Fig. 2 and Fig. 3, we select the summation of the Hankel singular values of the four dominant modes as the metric to determine the optimal single sensor

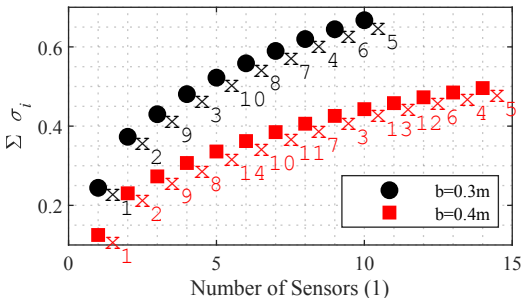

Fig. 4. Dependence of Hankel singular value summation of four dominant modes on number of sensors

placement. For case 1, the optimal sensor denoted as #1, is located at bottom x_1. Then the second optimal sensor location #2 is determined in a sequential scheme. For two-output systems, the first sensor is placed at x_1, the second #2 is chosen from the remaining available locations that ensures the largest Hankel singular value summation. With the second optimal sensor location determined, we can determine the third sensor in a similar manner. Based on this sequential optimization scheme, we find the optimal sensor combinations for any number of sensors.

With the above analysis, we obtain the dependence of the optimal Hankel singular value summation on the number of sensors, which is shown in Fig.4 for the two cases. The labels near the data points denote the sensor locations. x_1 means the bottom sensor and x_{10} means the sensor closet to the flame in case 1. The horizontal axis indicates the order of adding sensors for optimal overall mode observability. For instance, with three sensors available, the optimal combination of sensor locations is x_1, x_2, and x_9. The additional sensors will always increase the mode observability but with a diminishing trend.

4. EFFECT OF SENSOR PLACEMENT ON AN LQG CONTROLLER

4.1 Further Model Order Reduction

In this section, based on the state space model in modal realization form, we further truncate the model by neglecting the modes with extremely small Hankel singular values. Like the Fig. 2 and 3, only four dominant modes remain. Since the stable modes hardly modify the stability of the system, the sum of Hankel singular values from neglected unstable modes represent the truncation error. The truncation errors for the two cases are not greater than 2.5%.

After the further modal truncation, we achieve an eighth-order system with four acoustic modes. The Bode plots in Fig. 5 show the comparisons of the transfer function magnitude between the original ('Analytical') and truncated ('Truncated') systems observed at the bottom sensor location. The frequency response of the transfer function magnitude remains nearly the same at the four dominant modes and small differences exist at the other frequencies. The approximated system behaves similarly with the original system, at least near the acoustic resonant frequencies.

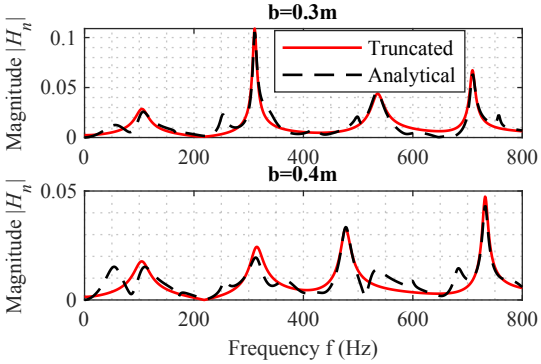

Fig. 5. Frequency response comparison between truncated and original systems at x_0=0.041m

4.2 LQG Controller Design

Based on the truncated systems, we design a Linear-Quadratic-Gaussian controller to suppress the pressure oscillation amplitude, included in the objective function defined in (10). In the cost function J, the weighting matrix Q_{xu} determines the optimization trade-off between input u effort minimization and output pressure oscillation attenuation. The definition of Q_{xu} is in (11). For simplicity, we assume no correlation exists between x and u. R is selected to be 1 and C is the output matrix in the state space form.

In the state space form of the system, we consider the existence of measurement noise v and process noise w. The weighting matrix Q_{wv} describes the covariance from the two noise sources. The intensities of Gaussian white noise sources w and v are selected to be $\delta^* = 5\times10^{-5}$ for the normalized output, which is approximately the ratio of the pressure measurement uncertainty $5Pa$ to the atmospheric pressure $1.013\times10^5 Pa$. The two noise sources are assumed to be independent with each other. In (12), N_x is the number of state variables in the state space model.

Based on the two weighting matrices Q_{xu} and Q_{wv}, we achieve the optimal LQG controller K_{lqg} that minimizes the cost function J defined in (10).

$$J = \frac{1}{t_{sim}} \int_0^{t_{sim}} \left[x^T, u^T\right] Q_{xu} \begin{bmatrix} x \\ u \end{bmatrix} dt \tag{10}$$

$$Q_{xu} = \begin{bmatrix} C^T C & \mathbf{0} \\ \mathbf{0} & R \end{bmatrix} \tag{11}$$

$$\begin{gathered} Q_{wv} = [\mathbf{w},\ \mathbf{v}] \cdot \left[\mathbf{w}^T \mathbf{v}^T\right] \\ \mathbf{w}^T = [\delta^*, \delta^*, ..., \delta^*, \delta^*]_{1\times N_x}, \mathbf{v}^T = \delta^* \end{gathered} \tag{12}$$

In this system, heat release response described by a linear time-lag model is proportional to the incoming velocity perturbation without any saturation limit. As a result, the open-loop thermoacoustic is linearly unstable, as seen by the open-loop output response to a unit impulse input in the left subplot of Fig. 6. The output oscillation amplitude increases with an exponential rate of $75.4 rad/s$. With the an LQG controller applied, the output of the closed-loop system for the same input now decays at a rate of -$16.4 rad/s$. The control input effort also decays in a similar

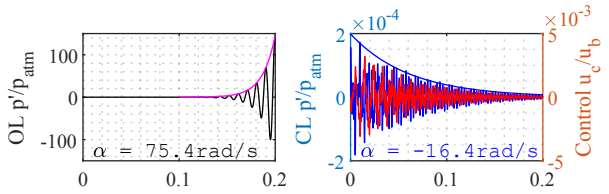

Fig. 6. Response of open- (left) and closed- (right) systems at b=0.3m and x_0=0.041m to a unit impulse input

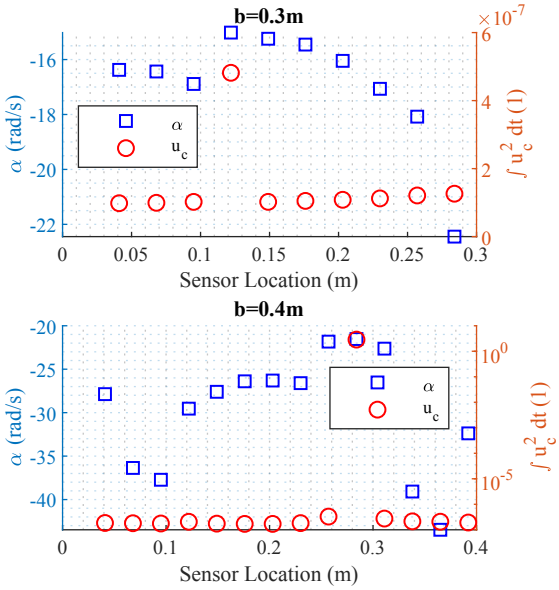

Fig. 7. Dependence of LQG controller's performance on sensor placement

way. We take the closed-loop output decay rate α and control input effort integration $\int u_c^2\,dt$ as the metrics for the LQG controller's performance.

4.3 Dependence of LQG Performance on Sensor Placement

In this section, we study the effects of sensor placement on the LQG controller's performance. Similar with the analysis for the case in Fig. 6, we place the single sensor at other locations and obtain the performance metrics for the corresponding LQG controller.

The dependence of the LQG controller's performance on the sensor placement is summarized in Fig. 7. The control effort is insensitive to sensor placement for most sensor locations. Much higher effort is observed at the location where nearly zero Hankel singular values are achieved. As shown in Fig.2 and Fig.3, the two locations are the fourth sensor in case 1 for the fourth mode and tenth sensor in case 2 for the second mode.

The decay rates are the smallest in magnitude at the above two extreme locations. It means the even with a higher control effort, the system is stabilized with a slower speed if the sensor is placed near some pressure nodes. In addition, the decay rate has a stronger dependence on the sensor placement than the control input effort. For example, the tenth sensor placement in case 1 and the thirteenth sensor placement in case 2 achieve a much faster decay of the pressure oscillations compared to the other locations even with similar control effort.

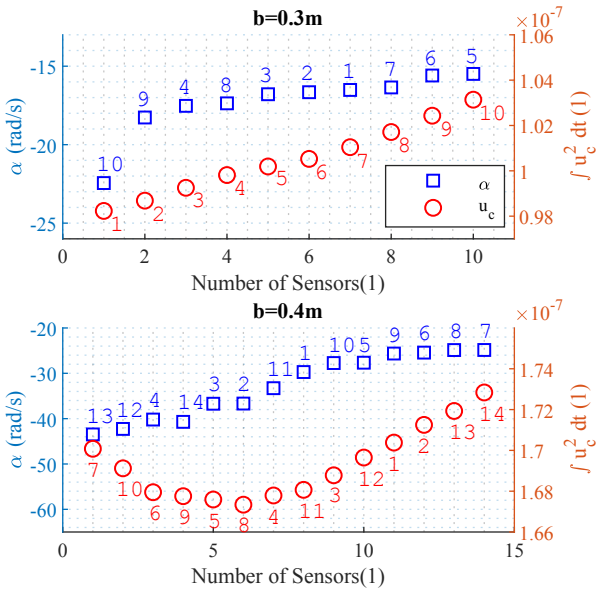

Fig. 8. Dependence of LQG controller's performance on number of sensors

4.4 Dependence of LQG Performance on Number of Sensors

Similar with analysis in section 3.4, we study the effects of multiple sensors on the LQG control performance. For the two metrics, we apply sequential optimization separately to obtain the sensor location combinations for different number of sensors.

In the circumstance of multiple outputs, the magnitude of each frequency component behaves differently at different sensor placements. As a result, the multiple outputs of the closed-loop system will decay at different rates. Among the multiple decay rates, we selected the one with the smallest magnitude as the optimal decay rate because the slowest decay process dominates the overall response. The dependence of LQG control performance on the number of sensors is summarized in Fig. 8.

In Fig. 8, numbers near the data points denote the sensor labels as that in Fig. 4. We see an increase of decay rates with the increasing number of sensors. This is because in a multi-output system, different frequency components contribute differently in the overall output due to the spatial pressure distribution variations. If we pick the slowest output decay rate among the multiple outputs as the performance evaluation metric, it is not surprising to see a relatively worse decay rate. There is also an increase of the control effort with more sensors applied, but with a much smaller trend.

Combining the analysis of the two performance metrics, we find that the LQG control with a single sensor already ensures a fast decay of combustion instability even with a small control input effort. Additional sensors fail improve the performance of the designed LQG controller.

4.5 Robustness Metric for LQG Controller

As shown in Table 1, both β and τ have uncertainties due to the sensor noise in the system identification. We assume that this is the only model uncertainties source

and neglect the uncertainties due to the modeling errors from Padé approximation or further order reductions. We represent the model uncertainties in the multiplicative form, as expressed in

$$\Delta_u = \frac{G_p - G_0}{G_0},\ G_p = (1 + \Delta_u)G_0 \tag{13}$$

where G_0 is the nominal transfer function determined by nominal parameters β_0 and τ_0, and G_p is the perturbed transfer function associated with uncertain parameters. The multiplicative uncertainty $\Delta_u(s)$ can be replaced by an upper bound weighting matrix $W_u(s)$, as follows

$$\Delta_u(s) = W_u(s)\Delta,\ \|\Delta\|_\infty \leq 1 \tag{14}$$

We assume that the two parameters vary within a range of 3σ level. The original transcendental weighting matrix $W_u(s)$ is approximated with a sixteenth-order frequency response fitting $W_{u,fit}(s)$. With a 3σ uncertainty level in parameters, the highest multiplicative uncertainty magnitude is near the fourth mode and the values are approximately 20% and 10% for case 1 and case 2, respectively.

With the determined uncertainty $W_{u,fit}(s)$, the perturbed system can be represented by the multiplicative transfer function H_{mult} as the following form. With the designed LQG control, the uncertain closed-loop system M is achieved by the linear fractional transform.

$$H_{mult} = \begin{bmatrix} 0 & W_u \\ G_0 & G_0 \end{bmatrix}, M = F_l(H_{mult}, -K_{lqg}) \tag{15}$$

The robustness of the controller can be evaluated by the structured singular value $\mu_\Delta(M)$ of the closed-loop system M, which describes the gain from disturbance to the error. With this metric, we analyze the dependence of the LQG controller's robustness on sensor placement in the following sections.

4.6 Dependence of LQG Robustness on Sensor Placement and Number of Sensors

As indicated in Fig. 9, most of the structured singular values of the system observed at different sensor placements are around 0.1, much smaller than one. This means the optimal LQG controller designed for the nominal plant G_0 can stabilize the perturbed systems with 3σ level of uncertainties in either one of the two parameters. This might because that the multiplicative uncertainty in the two examples are no more than 20%, which is small enough that nearly all the sensor placements achieve stability robustness. The special case is for the system with flame location at $0.3m$ and sensor placed at $0.122m$, where the structured singular value is about 0.4. This sensor location is near the pressure node of $709Hz$.

In situations with multiple sensors, we apply the same sequential optimization scheme for the optimal robustness - structured singular values. The dependence of the structured singular value for the system M on the number of sensors is shown in Fig.10. With multiple sensors, the robustness of the LQG controller can be improved to some extent but relation is not monotonous.

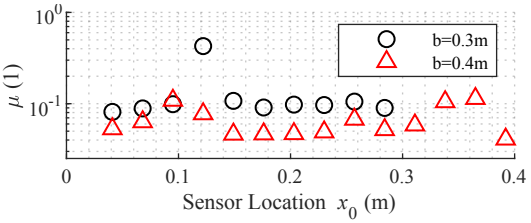

Fig. 9. Dependence of structured singular value on sensor placement for an LQG controller

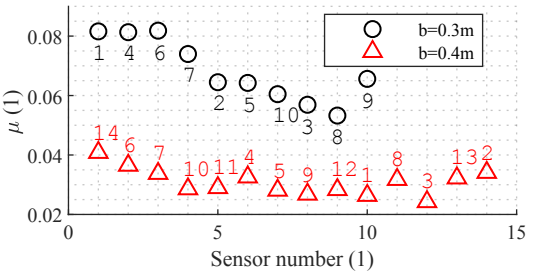

Fig. 10. Dependence of structured singular value on number of sensors for an LQG controller

5. CONCLUSIONS

This paper systematically studies the effect of sensor placement on the mode observability and performance of an LQG controller on a one-dimensional thermoacoustic model.

The method of placing sensor based on a Hankel singular value achieves similar conclusion with the literature that we should avoid placing the sensor near the pressure node positions. Additional sensor will always increase the Hankel singular values for both cases analyzed in this paper.

We design an optimal LQG controller to suppress the combustion instability of the reduced-order model with minimal output oscillation amplitude and control input effort. We select the output's exponential decay rate, control input effort, and the closed-loop system's structured singular value as the evaluate metrics. We analyze the effects of the sensor placement and the number of sensors on the above performance and robustness metrics. The conclusions are summarized as follows:

(1) Output decay rates vary strongly with the sensor placement while the control effort nearly keeps as constant.
(2) Similar to the small Hankel singular values observed at pressure nodes, low decay rates and high control efforts appear when the sensors are placed near the pressure nodes.
(3) Similar to both decay rate and control input effort, structured singular values of the closed-loop system μ are almost independent with the sensor placement, except for higher values achieved at some pressure nodes.
(4) Additional sensors will not significantly change the control input effort, but slightly worsen the thermoacoustic instability damping.

(5) Additional sensors will improve the robustness of the LQG controller but the magnitude of improvement varies between the two different flame locations.

ACKNOWLEDGEMENTS

This material is based upon work supported by the National Science Foundation under Grant No.e CMMI-1728307. Any opinions, findings, and conclusions or recommendations expressed in this material are those of the authors and do not necessarily reflect the views of the National Science Foundation.

REFERENCES

Annaswamy, A.M., Fleifil, M., Rumsey, J.W., Prasanth, R., Hathout, J.P., and Ghoniem, A.F. (2000). Thermoacoustic instability: model-based optimal control designs and experimental validation. *IEEE Transactions on Control Systems Technology*, 8(6), 905–918.

Annaswamy, A.M. and Ghoniem, A.F. (1995). Active control in combustion systems. *IEEE Control Systems Magazine*, 15(6), 49–63.

Barooah, P., Anderson, T.J., and Cohen, J.M. (2003). Active combustion instability control with spinning valve actuator. *J. Eng. Gas Turbines Power*, 125(4), 925–932.

Bloxsidge, G., Dowling, A., Hooper, N., and Langhorne, P. (1988). Active control of reheat buzz. *AIAA journal*, 26(7), 783–790.

Bothien, M.R., Moeck, J.P., and Paschereit, C.O. (2008). Active control of the acoustic boundary conditions of combustion test rigs. *Journal of Sound and Vibration*, 318(4-5), 678–701.

Celik, M., Ocali, O., Tan, M.A., and Atalar, A. (1995). Pole-zero computation in microwave circuits using multipoint padé approximation. *IEEE Transactions on Circuits and Systems I: Fundamental Theory and Applications*, 42(1), 6–13.

Chen, X., Dillen, E., Fathy, H., and O'Connor, J. (2019). Optimizing the design of a rijke tube experiment for combustion stability model identifiability. In *2019 American Control Conference (ACC)*, 4974–4981. IEEE.

Crocco, L. and Cheng, S.I. (1956). Theory of combustion instability in liquid propellant rocket motors. Technical report, Princeton University NJ.

Dines, P.J. (1984). *Active Control of Flame Noise*. Ph.D. thesis, University of Cambridge.

Hathout, J., Annaswamy, A., Fleifil, M., and Ghoniem, A. (1998). A model-based active control design for thermoacoustic instability. *Combustion science and technology*, 132(1-6), 99–138.

Heckl, M.A. (1988). Active control of the noise from a rijke tube. *Journal of Sound and Vibration*, 124(1), 117–133.

Hermann, J., Orthmann, A., and Hoffmann, S. (1999). Active instability control of combustion oscillations in heavy duty gas turbines. In *6th International Congress on Sound and Vibration, Copenhagen, Denmark*.

Lang, W., Poinsot, T., and Candel, S. (1987). Active control of combustion instability. *Combustion and Flame*, 70(3), 281–289.

Langhorne, P., Dowling, A., and Hooper, N. (1990). Practical active control system for combustion oscillations. *Journal of Propulsion and Power*, 6(3), 324–333.

Lieuwen, T., Torres, H., Johnson, C., and Zinn, B.T. (1999). A mechanism of combustion instability in lean premixed gas turbine combustors. *Journal of Engineering for Gas Turbines and Power*, 123(1), 182–189.

Lieuwen, T.C. and Yang, V. (2005). *Combustion instabilities in gas turbine engines: operational experience, fundamental mechanisms, and modeling*. American Institute of Aeronautics and Astronautics.

Nagar, S. and Singh, S. (2004). An algorithmic approach for system decomposition and balanced realized model reduction. *Journal of the Franklin Institute*, 341(7), 615–630.

Poinsot, T., Candel, S., Esposito, E., Lang, W., and Bourienne, F. (1989). Suppression of combustion instabilities by active control. *Journal of Propulsion and Power*, 5(1), 14–20.

Richards, G.A., Straub, D.L., and Robey, E.H. (2003). Passive control of combustion dynamics in stationary gas turbines. *Journal of Propulsion and Power*, 19(5), 795–810.

Seume, J., Vortmeyer, N., Krause, W., Hermann, J., Hantschk, C.C., Zangl, P., Gleis, S., Vortmeyer, D., and Orthmann, A. (1997). Application of active combustion instability control to a heavy duty gas turbine. In *ASME 1997 Turbo Asia Conference*, V001T05A007–V001T05A007. American Society of Mechanical Engineers.

Sharma, A. and Fathy, H.K. (2014). Fisher identifiability analysis for a periodically-excited equivalent-circuit lithium-ion battery model. *Proceedings of the American Control Conference*, 274–280.

Yang, V., Sinha, A., and Fung, Y.T. (1992). State-feedback control of longitudinal combustion instabilities. *Journal of Propulsion and Power*, 8(1), 66–73.

Zhao, D. and Li, J. (2012). Feedback control of combustion instabilities using a helmholtz resonator with an oscillating volume. *Combustion Science and Technology*, 184(5), 694–716.

Zhou, K., Salomon, G., and Wu, E. (1999). Balanced realization and model reduction for unstable systems. *International Journal of Robust and Nonlinear Control: IFAC-Affiliated Journal*, 9(3), 183–198.

Appendix A. TERMS IN THE TRANSFER FUNCTIONS (7) AND (8)

$$e_{13} = \frac{\bar{\rho}_m \bar{c}_m e^{t_1 s} + \bar{\rho}_n \bar{c}_n e^{t_3 s}}{\bar{\rho}_1 \bar{c}_1}$$
$$e_{24} = \frac{\bar{\rho}_m \bar{c}_m e^{t_2 s} + \bar{\rho}_n \bar{c}_n e^{t_4 s}}{\bar{\rho}_1 \bar{c}_1} \tag{A.1}$$

$$\bar{\rho}_m \bar{c}_m = \bar{\rho}_1 \bar{c}_1 + (1 - \beta e^{-\tau s}) \bar{\rho}_2 \bar{c}_2$$
$$\bar{\rho}_n \bar{c}_n = \bar{\rho}_1 \bar{c}_1 - (1 - \beta e^{-\tau s}) \bar{\rho}_2 \bar{c}_2$$
$$t_1 = \frac{b}{\bar{c}_2} + \tau, t_3 = \frac{(2L - b)}{\bar{c}_2} + \tau \tag{A.2}$$
$$t_2 = \frac{2b}{\bar{c}_1} + t_3, t_4 = \frac{2b}{\bar{c}_1} + t_1, t_5 = \frac{b}{\bar{c}_1} + \tau$$

$$e_m = e^{t_1 s} + e^{t_2 s}, e_n = e^{t_3 s} + e^{t_4 s} \tag{A.3}$$